The azide-alkyne cycloaddition catalysed by transition metal oxide nanoparticles

Giorgio Molteni,[a]* Anna M. Ferretti,[b] Mario Italo Trioni,[c] Fausto Cargnoni,[c] Alessandro Ponti[b]*

[a] Dipartimento di Chimica, Università degli Studi di Milano, via C. Golgi 19, 20133 Milano, Italy.

[b] Laboratorio di Nanotecnologie, Istituto di Scienze e Tecnologie Molecolari (ISTM), Consiglio Nazionale delle Ricerche, via G. Fantoli 16/15, 20138 Milano, Italy.

[c] Istituto di Scienze e Tecnologie Molecolari (ISTM), Consiglio Nazionale delle Ricerche, via C. Golgi 19, 20133 Milano, Italy.

* Corresponding Authors

Dr. A. Ponti: alessandro.ponti@istm.cnr.it

Dr. G. Molteni: giorgio.molteni@unimi.it

Abstract: Colloidal nanoparticles of Earth-abundant, first-row transition metal oxides and sulfide, namely magnetite (Fe_3O_4), manganese and cobalt ferrite, ($MnFe_2O_4$, $CoFe_2O_4$), manganese(II) oxide (MnO) and sulfide (α-MnS), were used as catalysts in the cycloaddition between azides and methyl propiolate. The presence of these nanoparticles allowed us to carry out the cycloadditions at milder conditions and with a regioselectivity comparable to the classic "metal-free" thermal processes. Ferrite nanoparticles gave higher conversion than MnO and α-MnS nanoparticles. The feasibility of the cycloaddition onto 1,2-disubstituted acetylenes was also proved. Ferrite nanocatalysts could be magnetically recovered and reused without significant loss of catalytic activity. Density functional theory (DFT) calculations support a mechanistic hypothesis that attributes the increased cycloaddition rate to the adsorption of the azide onto to the nanocatalyst surface.

Keywords. Cycloaddition, azide, alkyne, 1,2,3-triazole, nanoparticle, ferrite.

1. Introduction

Catalysis by inorganic nanoparticles (NPs) is a very rapidly growing field [1] since catalytically active NPs may combine the advantages and overcome the shortcomings of the homogeneous and heterogeneous approaches to catalysis.[2] NP catalysts are robust, easily recoverable and recyclable, like heterogeneous catalysts. Colloidal NPs – as opposed to supported NPs – are well dispersed within the reaction medium, thus increasing the available catalytic surface and improving the diffusion of reactants and products, though they cannot achieve the unimpeded mass transfer and high accessibility of active sites typical of homogeneous catalysts.

The choice route to the 1,2,3-triazole ring is provided by the azide-alkyne cycloaddition.[3] Although such a reaction dates to the end of the 19th century,[4] its mechanism and synthetic applications were disclosed by Huisgen in the early 1960s.[5,6,7] Forty years later, the concept of "click" reaction allowed for the first time the fully regioselective cycloaddition to 4-substituted-1,2,3-triazoles.[8,9] Quite recently, novel homogeneous metallorganic catalysts accomplished the regioselective synthesis of the 5-substituted, complementary isomer.[10,11,12,13,14] Due to its robustness, it is fair to say that the azide-alkyne cycloaddition has assumed a prominent position at the interface between chemistry, biology, and materials science.[15,16] As examples, some derivatives of 1,2,3-triazoles are effective drugs against epilepsy [17] and diabetes,[18] and 1,2,3-triazolium-containing ionic liquids containing mixed polymeric materials are of great interest as immobilised catalysts.[19]

In 2006, some of us introduced the use of colloidal Cu@Cu$_2$O|CuO NPs as effective catalysts for the cycloaddition of organic azides and terminal alkynes to 1,2,3-triazoles.[20] Several examples followed, [21,22,23] which involved colloidal Cu,[24,25] Fe@Cu,[26] Cu$_2$O,[27,28] CuO,[29] and CuFe$_2$O$_4$ [30,31] NPs, in some cases extending this approach to aqueous solvents.[24,26,27,29,31] In these reactions, the 4-substituted triazole is formed and internal alkynes do not react, as in the homogeneous copper-catalysed 'click' reaction. The NP-catalysed mechanism was shown to be similar [32] to that of the homogeneous reaction.[33] Ag$_2$O NPs also catalyse this cycloaddition but the mechanism seems different as electron-poor azides gave a mixture of the 4- and 5-substituted isomers.[34]

We then turned our attention to cheaper metals as possible nanocatalysts for the azide-alkyne cycloaddition. We selected in particular iron as an abundant, inexpensive, environmentally friendly and biocompatible metal and focused on its oxide Fe$_3$O$_4$ (magnetite) for its robustness, stability and magnetization, which makes magnetite nanocatalysts easy to recover by an external magnet.[35] Colloidal iron oxide NPs catalyse a number of organic reactions, mainly oxidations [1,35] but also polymerization,[36] isomerization,[37,38] hydrogenation,[39] alkylation and alkenylation,[1] and reactions involving the oxidative activation of the C–H bond.[35] We have recently shown that magnetite NPs are good catalysts for the cycloaddition of nitrilimines to alkenes, alkynes, and activated nitriles.[40] To widen the scope of our

investigation about azide-alkyne cycloaddition, we also considered the iron neighbours manganese and cobalt, despite their slightly higher impact on health and environment. This, in addition to magnetite NPs, we considered NPs made of either mixed ferrite ($MnFe_2O_4$, $CoFe_2O_4$) and manganese(II) oxide (MnO) and sulfide (α-MnS). The Mn and Co ferrite NPs have found use as catalysts for organic reactions.[41,42] Here we show that colloidal magnetite NPs – along with Mn and Co ferrite, Mn(II) oxide and sulfide NPs – are effective catalysts for the cycloaddition between organic azides and both terminal and internal alkynes.

2. Experimental section

Synthesis of iron oxide (Fe_3O_4) nanoparticles

Fe_3O_4 nanoparticles were synthesized by modification of a reported procedure.[43] In a 50-ml three-necked round-bottom flask, equipped with condenser, thermocouple, and rubber septum, oleic acid (OlAc, 2.4 ml, 7.5 mmol) was dissolved in 10 ml of octadec-1-ene (ODE) under stirring and argon atmosphere. The solution was heated to 105 °C and degassed three times by vacuum-argon cycles. After 40 min. $Fe(CO)_5$ (330 μl, 2.5 mmol) was injected through the rubber septum. The reaction mixture was heated to 320 °C (heating rate 15 °C/min) and aged at that temperature for 3 h. After cooling at RT, the reaction crude was precipitated with acetone and the nanoparticles were collected by centrifugation (3400 g, 10 min). The nanoparticles were repeatedly washed with acetone and collected by centrifugation (3400 g, 10 min). The resulting OlAc-coated NPs were dispersed in toluene at a concentration of 3.22 g_{Fe}/l. The isolated yield was 58% with respect to $Fe(CO)_5$.

Synthesis of mixed ferrite (MFe_2O_4, M = Mn, Co) nanoparticles

MFe_2O_4 nanoparticles were synthesized following of a reported procedure [44] except for the use of 1,2-hexadecanediol instead of 1,2-tetradecanediol. The molar ratio $M(acac)_2$:$Fe(acac)_3$ was 1:2 (acac = acetylacetonate). In a 100-ml three-necked round-bottom flask, equipped with condenser, thermocouple, and rubber septum, oleic acid (OlAc, 1.0 ml, 3.15 mmol), oleylamine (1.0 ml, 3.04 mmol), $Fe(acac)_3$ (0.350 g, 0.990 mmol), and $M(acac)_2$ (0.495 mmol, M = Mn, Co) were dissolved in 25 ml of dibenzylether under stirring and argon atmosphere. The reaction mixture was rapidly heated to 120 °C and held at that temperature for 30 min under vacuum and 30 min under argon. Next, it was heated to 210 °C (heating rate: 8 °C/min) and held at that temperature for 2 h under argon. Finally, the reaction mixture

3

was heated to 300 °C (heating rate: 3 °C/min) and aged at that temperature for 1 h. After the high temperature synthesis, the nanoparticles were washed 5 times with acetone/ethanol mixture and collected by centrifugation (3400 g, 10 min). The resulting nanoparticles were dispersed in toluene at a concentration 2.16 g_{Fe}/l ($MnFe_2O_4$) and 2.31 g_{Fe}/l ($CoFe_2O_4$). The isolated yield was about 30% with respect to $Fe(acac)_3$.

Synthesis of manganese(II) oxide (MnO) and manganese(II) sulfide (α-MnS) nanoparticles

MnO and α-MnS nanoparticles were synthesized adapting reported procedures.[45] The actual procedure for MnO and α-MnS nanoparticles is as follows. In a 25-ml two-necked round-bottom flask, equipped with condenser, thermocouple, $Mn_2(CO)_{10}$ (104 mg, 0.267 mmol), stearic acid (StAc, 448 mg, 1.57 mmol), and elemental sulfur (34 mg, 1.1 mmol) was dissolved in 1.1 ml of octadec-1-ene (ODE) under stirring and argon atmosphere. The solution was heated to 320 °C (heating rate 10 °C/min) and aged at that temperature for 1 h. After cooling at RT, the solid reaction crude was dissolved in about 3 ml of toluene and added with 12 ml of ethanol. The nanoparticles were collected by centrifugation (3400 g, 10 min) after adding. Next, the nanoparticles were washed with ethanol (5 %) and acetone (x 2) collected and by centrifugation (3400 g, 10 min). Extensive washing is required to eliminate the excess stearic acid. The resulting StAc-coated MnO nanoparticles were dispersed in n-hexane at a concentration of 1.21 g_{Mn}/l. To obtain α-MnS nanoparticles, the above procedure was followed dissolving $Mn_2(CO)_{10}$ (107 mg, 0.273 mmol), stearic acid (StAc, 298 mg, 1.05 mmol), and elemental sulfur (68 mg, 2.1 mmol) in 1.1 ml of ODE. The resulting StAc-coated α-MnS nanoparticles were dispersed in n-hexane at a concentration of 1.05 g_{Mn}/l.

Cycloaddition between azides 1 and methyl propiolate in the presence of CuI. General procedure

A solution of azide **1** (0.5 mmol) and methyl propiolate (84 mg, 1.0 mmol) in dry toluene (2.0 ml) was added with CuI (190 mg, 1.0 mmol). The heterogeneous mixture was stirred at 20°C and the reaction was monitored with periodic TLC (hexane/ethyl acetate 7:3). After 9 h (**4a**, $R_f = 0.35$), 18 h (**4b**, $R_f = 0.13$) or 6 h (**4c**, $R_f = 0.28$), the undissolved material was filtered over a celite pad and washed with acetone (3 x 2 ml). The collected solvents were evaporated under reduced pressure and the residue was crystallized with diisopropyl ether affording 4-substituted-1,2,3-triazoles **4a-c**.

Uncatalysed cycloaddition between azides 1 and methyl propiolate 2. General procedure

A solution of azide **1** (0.5 mmol) and methyl propiolate (67 mg, 0.8 mmol) in dry toluene (2.0 ml) was stirred at the temperatures and the times listed in the Tables 3 and 4. The reactions were monitored by

TLC (hexane/ethyl acetate 7 : 3). The solvent was removed under reduced pressure and the residue was chromatographed on a silica gel column with hexane/ethyl acetate 7 : 3.

In the case of the reaction carried out at 20°C (Table 3, entry 1), unchanged **1a** was eluted first (83 mg, 55%). Further elution gave 5-substituted-1,2,3-triazole **5a** (R_f = 0.46) and 4-substituted-1,2,3-triazole **4a** (44 mg, 23%).

In the case of the reaction carried out at 75°C (Table 4, entry 1), **5b** (R_f = 0.37) was eluted first, followed by **4b** (67 mg, 64%).

In the case of the reaction carried out at 90°C (Table 4, entry 7), **5c** (R_f = 0.56) was eluted first, followed by **4c** (75 mg, 74%).

Cycloaddition between azides 1 and methyl propiolate 2 in the presence of Fe_3O_4 nanoparticles

A solution of azide **1** (0.5 mmol), methyl propiolate (67 mg, 0.8 mmol) and Fe_3O_4 nanoparticles (1 ml, 58 μmol of Fe) in toluene (1.0 ml) was stirred at the temperatures and the times listed in the Tables 3 and 4. The reaction crude was filtered over a celite pad and washed with ethyl acetate (3 x 3 ml). The collected solvents were evaporated under reduced pressure.

In the case of the reaction carried out at 20°C (Table 3, entry 4), the residue was chromatographed on a silica gel column with hexane/ethyl acetate 7 : 3. Unchanged **1a** was eluted first (60 mg, 40%). Further elution gave a mixture of 1,2,3-triazoles **4a** and **5a** (110 mg, 57%) in the ratio 65 : 35 as determined by ^{1}H NMR.

In the case of the reactions carried out at 45°C (Table 3, entry 5 and Table 4, entries 2 and 8), 75°C (Table 3, entry 6) and 95°C (Table 3, entry 7) the ratio **4** : **5** was determined by ^{1}H NMR.

Cycloaddition between azides 1 and methyl propiolate 2 in the presence of $CoFe_2O_4$ nanoparticles

A solution of azide **1** (0.5 mmol), methyl propiolate (67 mg, 0.8 mmol) and $CoFe_2O_4$ nanoparticles (0.66 ml, 27 μmol of Fe, 10 μmol of Co) in toluene (1.34 ml) was stirred at 45°C for the times listed in Tables 3, entry 8 and Table 4, entries 3 and 9. The reaction crude was filtered over a celite pad and washed with ethyl acetate (3 x 3 ml). The collected solvents were evaporated under reduced pressure.

The ratio **4** : **5** was determined by ^{1}H NMR of the residue.

Cycloaddition between azides 1 and methyl propiolate 2 in the presence of $MnFe_2O_4$ nanoparticles

A solution of azide **1** (0.5 mmol), methyl propiolate (67 mg, 0.8 mmol) and $MnFe_2O_4$ nanoparticles (0.45 ml, 17 μmol of Fe, 6 μmol of Mn) in toluene (1.55 ml) was stirred at 45°C for the times listed in Tables 3, entry 9 and Table 4, entries 4 and 10. The reaction crude was filtered over a celite pad and washed with ethyl acetate (3 x 3 ml). The collected solvents were evaporated under reduced pressure.

The ratio **4** : **5** was determined by ^{1}H NMR of the residue.

Cycloaddition between azides 1 and methyl propiolate 2 in the presence of MnO nanoparticles

A solution of azide **1** (0.5 mmol), methyl propiolate (67 mg, 0.8 mmol) and MnO nanoparticles (0.45 ml, 10 µmol of Mn) in toluene (1.55 ml) was stirred at 45°C for the times listed in Tables 3, entry 10 and Table 4, entries 5 and 11. The reaction crude was filtered over a celite pad and washed with ethyl acetate (3 x 3 ml). The collected solvents were evaporated under reduced pressure.

The ratio **4** : **5** was determined by ^{1}H NMR of the residue.

Cycloaddition between azides 1 and methyl propiolate 2 in the presence of MnS nanoparticles

A solution of azide **1** (0.5 mmol), methyl propiolate (67 mg, 0.8 mmol) and MnS nanoparticles (0.45 ml, 8 µmol of Mn) in toluene (1.55 ml) was stirred at 45°C for the times listed in Tables 4, entry 11 and Table 4, entries 6 and 12. The reaction crude was filtered over a celite pad and washed with ethyl acetate (3 x 3 ml). The collected solvents were evaporated under reduced pressure.

The ratio **4** : **5** was determined by ^{1}H NMR of the residue.

Uncatalysed cycloaddition between azide 1a and DMAD 3

A solution of azide **1a** (0.15 g, 0.5 mmol) and DMAD **3** (0.14 g, 1.0 mmol) in toluene (2.0 ml) was stirred at the temperatures and the times listed in the Table 5. The reactions were monitored by TLC (hexane/ethyl acetate 7 : 3). Evaporation of the solvent gave a residue which was crystallized with diisopropyl ether affording pure **6** (R_f = 0.6), reaction at 20°C: 0.16 g, 72%; reaction at 95°C: 0.22 mg, 99%.

Cycloaddition between azide 1a and DMAD 3 in the presence of Fe$_3$O$_4$ nanoparticles

A solution of azide **1a** (0.15 g, 0.5 mmol), DMAD (0.14 g, 1.0 mmol) and Fe$_3$O$_4$ nanoparticles (0.25 ml, 14 µmol of Fe) in toluene (1.75 ml) was stirred at the temperatures and the times listed in the Table 5. Evaporation of the solvent gave a residue which was crystallized with diisopropyl ether affording pure **6** (reaction at 20°C: 0.22 g, 99%, reaction at 95°C: 0.22 mg, 99%).

Cycloaddition between azide 1a and DMAD 3 in the presence of MnFe$_2$O$_4$ nanoparticles

A solution of azide **1a** (0.15 g, 0.5 mmol), DMAD (0.14 g, 1.0 mmol) and MnFe$_2$O$_4$ nanoparticles (0.44 ml, 17 µmol of Fe, 6 µmol of Mn) in toluene (1.56 ml) was stirred at 20°C for 20 h. Evaporation of the solvent gave a residue which was crystallized with diisopropyl ether affording pure **6** (0.20 g, 91%).

Recycling of the Fe_3O_4 NP catalyst in the cycloaddition between azide 1c and methyl propiolate 2.

The recycling experiments were carried out using dichloromethane as a solvent because it is easier to keep the reaction temperature constant and to isolate products and NPs.

First run. In a 100 mL cylindrical reaction funnel, phenylazide **1c** (0.50 g, 4.2 mmol) and methyl propiolate **2** (0.38 g, 4.5 mmol) were dissolved in dry dichloromethane (16.3 mL). Fe_3O_4 NPs (47 mg, 0.84 mmol of Fe) dispersed in chloroform (4.7 mL) were added dropwise in 2 min. The mixture was submitted to vigorous magnetic stirring for 6 h at 40°C. The undissolved material was recovered with an external magnet, washed with dichloromethane (8 mL) and recovered again with an external magnet. The mother solution was washed with water (3 x 25 mL), dried over sodium sulfate and evaporated under reduced pressure. The crude was crystallised with diisopropyl ether giving a mixture of the isomeric triazoles **4a** + **5a** (0.76 g, 89%).

Subsequent runs (2nd-5th). The recovered NPs were dispersed in dry dichloromethane (21 mL) and amounts of **1c** and **2** were added as in the first run. After 6 h at 40°C, the isomeric triazoles were isolated and the NPs recovered and washed as in the first run.

The recycling experiments where the NP mass after each run was measured were carried out as above except that the recovered NPs were dried with a rotary pump (0.05 mmHg) for 1 h and weighted before dispersion in dichloromethane for the next cycle.

Characterization.

Transmission electron microscopy (TEM) images and electron diffraction (ED) patterns were collected using a Zeiss LIBRA 200FE microscope. The TEM specimen was prepared by evaporating in air a drop of diluted NP dispersion on a carbon coated copper grid. The size distribution of the iron oxide cores was obtained analysing TEM images by the software PEBBLES.[51] PEBBLES is freely available from the authors (http://pebbles.istm.cnr.it). FT-IR spectra were collected using a Thermo Nicolet NEXUS 670 FTIR spectrometer. The specimen for FTIR was prepared by grinding and pelleting dry NPs with KBr (NP:KBr 1:100 w/w). ^{1}H NMR (300 MHz) and ^{13}C NMR (75 MHz) spectra were taken with a Bruker Fourier 300 spectrometer (in $CDCl_3$ solutions at room temperature). Chemical shifts are given as parts per million from tetramethylsilane. Coupling constants (*J*) values are given in hertz and are quoted to ±0.1 Hz consistently with NMR machine accuracy. Element analyses were carried out by a Perkin-Elmer 2400 series II CHNS/O Analyzer.

Computational methods.

Periodic Density Functional (DFT) computations were carried out by the SIESTA 4.0 suite of programs. [46] The surface of a magnetite nanoparticle was simulated as a two-dimensional supercell reproducing the

7

stoichiometry of the bulk compound. In the case of the (100) slab the cell contains 62 atoms plus one **1c** molecule. In both systems the **1c** moiety is adsorbed onto an under-coordinated surface Fe atom. The surface unit cells was designed such that the overall stoichiometry reproduced the oxygen to iron ratio of the bulk material. When necessary, surface atoms were saturated with -H and -OH groups to reproduce their formal oxidation state. DFT computations were conducted with the PBE exchange and correlation functionals. In accordance with literature results,[47] we included also a *U* term for Fe atoms, amounting to 4 eV, to reproduce at best the DOS of bulk Fe_3O_4. All atoms except hydrogen were assigned a split-valence basis set of double zeta quality for valence electrons, while norm-conserving Troullier-Martins pseudopotentials were adopted to describe the core electrons. The reciprocal space was sampled with a 8×8 *k*-points grid. Convergence of the wavefunction was facilitated by imposing an electronic temperature of 300 K within a Fermi-Dirac occupation statistics. All geometries were fully optimized. Figure 7 compares energies belonging to different computations, i.e. having different vacuum energy levels, and hence the DOS of **1c** and energy levels of **2** were aligned so that the distance between the lowest eigenvalues shown in the figure reproduces the value obtained in a gas phase computation including both molecules in a non-interacting configuration.

Molecular DFT calculations related to the cycloaddition of **2** and **1c**, **1c**-Fe(OH)$_3$ and **1c**-Fe$_2$(OH)$_4$ were carried using the OPBE functional, which was shown to perform well with Fe(III) complexes,[48] the LANL2 pseudopotential, and the LANL2DZ basis set as implemented in the Gaussian09 Suite.[49] All geometries were fully optimized and harmonic analysis showed that they were true energy minima (no imaginary frequency) or transition states (one imaginary frequency), as required.

3. Results and discussion

3.1 Nanoparticles synthesis and characterization

Transition metal oxides (Fe_3O_4, $MnFe_2O_4$, $CoFe_2O_4$, MnO) and α-MnS NPs were synthesized by the solvothermal decomposition of the appropriate precursors as detailed in the Experimental section. All NPs used in this study consist of a nanocrystal coated with a layer of fatty acid and are colloidally stable in apolar solvents. The main features of the NPs are collected in Table 1. The concentration of Fe (ferrites) and that of Mn (MnO and MnS) in the NP dispersions were obtained by spectrophotometry [50] and chemical analysis (see ESI), respectively.

Table 1. Main features of as-synthesized metal oxide and sulfide nanoparticles.

NP	C_{Fe} (g/l)	C_M (g/l)	Dispersion solvent	Coating	$<d>$ [a]	σ_d [b]	$\sigma_d/<d>$ (%)
Fe_3O_4	3.22	—	toluene	oleic acid	11.9	0.6	5
$CoFe_2O_4$ [c]	2.31	0.85 (Co)	toluene	oleic acid	10	2.0	20
$MnFe_2O_4$	2.16	0.73 (Mn)	toluene	oleic acid	8.6	1.2	14
MnO	—	1.21 (Mn)	n-hexane	stearic acid	11.6	1.6	14
α-MnS	—	1.05 (Mn)	n-hexane	stearic acid	44	12	27

[a] Median equivalent diameter (nm). [b] Diameter standard deviation (nm). [c] $CoFe_2O_4$ NPs have elongated shape with major axis = (12 ± 3) nm (24%), minor axis = (9 ± 2) nm (20%), aspect ratio = (1.3 ± 0.2) (15 %).

Transmission electron microscopy (TEM) images of as-synthesized NPs can be found in Figure 1(a-e) (wide field TEM images can be found in the ESI, Figure S1). The size distribution of the NPs (see ESI, Figure S2) was obtained by analysing TEM images by the software PEBBLES.[51] Magnetite NPs are spherical and have a very small size dispersion. Manganese (spherical) and cobalt (irregular) ferrite NPs are slightly smaller and have larger size dispersion. Both are slightly deficient in the divalent metal, as evidenced by electron energy loss spectroscopy (EELS). Their composition can be expressed as $Co_{0.78}Fe_{2.22}O_4$ and $Mn_{0.77}Fe_{2.23}O_4$. Octahedral MnO NPs are similar in size to Fe_3O_4 NPs but have larger size dispersion. α-MnS NPs are much larger and have spheroidal shape. Electron diffraction (Figure 2) allowed us to identify the nanocrystals as cubic ferrites (spinel structure) Fe_3O_4, $CoFe_2O_4$, $MnFe_2O_4$ and as rock-salt structure MnO and α-MnS. It should however be noted that the poor resolution of the diffraction pattern prevented us to distinguish between magnetite (Fe_3O_4) and maghemite (γ-Fe_2O_3), so that partial oxidation of magnetite NPs cannot be excluded.
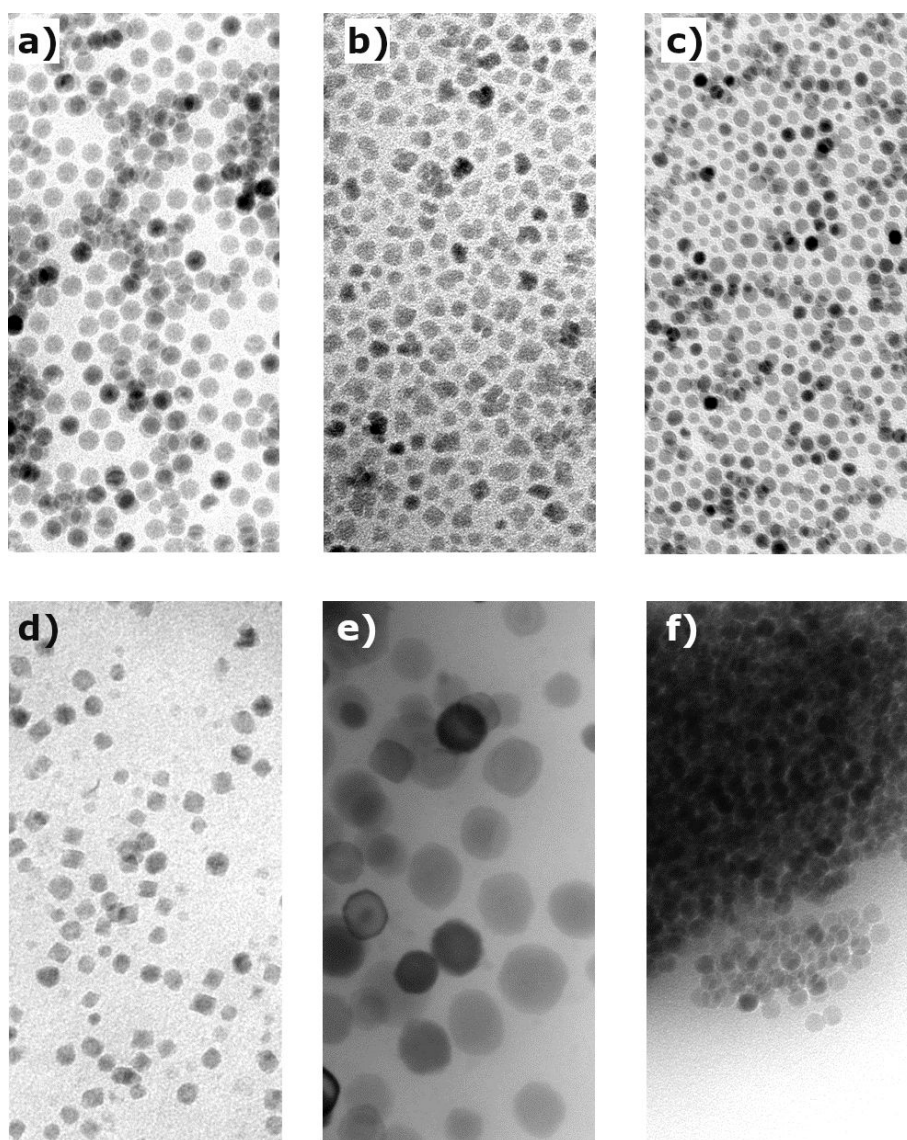
Figure 1. TEM images of as-synthesized (a-e) and used (f) nanoparticles. a) Fe_3O_4; b) $CoFe_2O_4$; c) $MnFe_2O_4$; d) MnO; e) α-MnS; f) Fe_3O_4 after 5 runs.
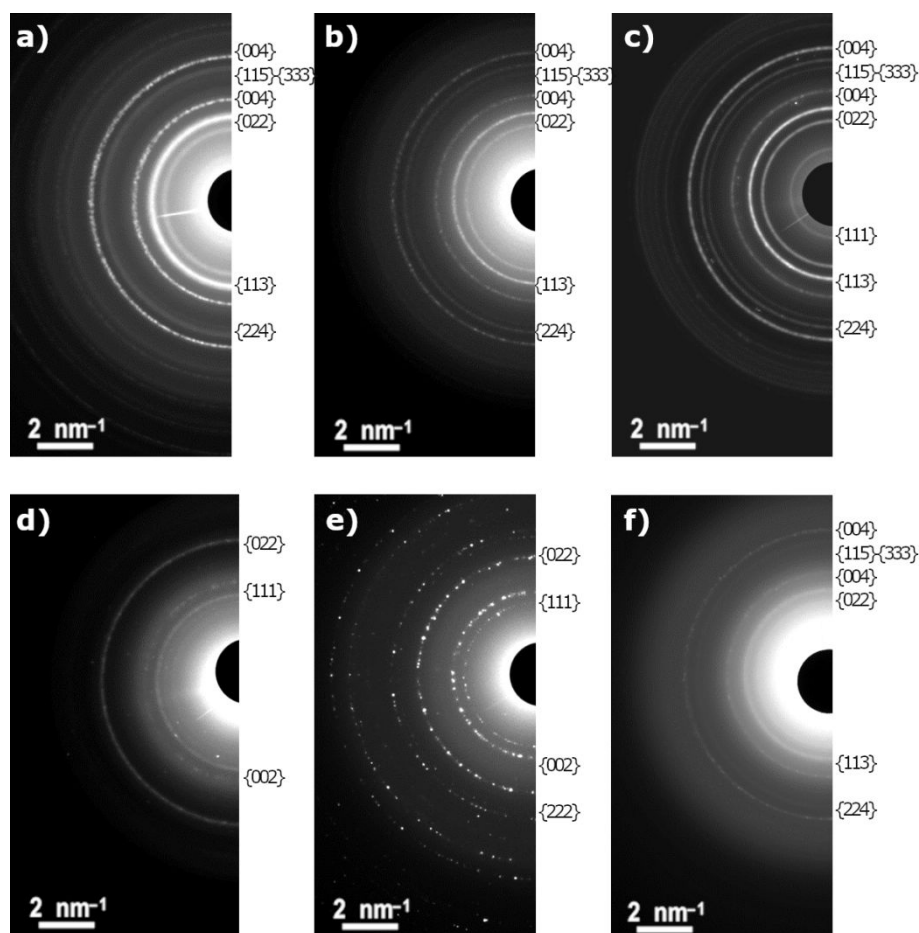
Figure 2. Electron diffraction patterns of as-synthesized (a-e) and used (f) nanoparticles. a) Fe_3O_4; b) $CoFe_2O_4$; c) $MnFe_2O_4$; d) MnO; e) α-MnS; f) Fe_3O_4 after 5 runs. Patterns in a), b), c) and f) are consistent with the spinel structure; patterns in d) and e) are consistent with the rock-salt structure

The FT-IR spectra of the NPs confirmed that they are coated with a layer of fatty acid in the carboxylate form. The spectra of Fe_3O_4 and α-MnS NPs are shown in Figure 3 as examples of NPs coated with oleic and stearic acid, respectively. Both spectra display the characteristic peaks of fatty acid anions: the C-H stretching vibration of CH_2 and CH_3 groups (2956-2851 cm^{-1}) and the symmetric and asymmetric stretches of the COO^- group (ca. 1550 and 1430 cm^{-1}). The weak peak at 3004 cm^{-1} (C-H stretching of sp^2 carbon) and the strong peak at 590 cm^{-1} (Fe-O stretching) are only present in the spectrum of oleic acid coated Fe_3O_4 NPs. The density of the fatty acid ligands on the NP surface affects both the number of catalytic sites and the ease by which the reactants and products can diffuse to and from the NP. The ligand density collected in Table 2 were calculated by dividing the amount of fatty acid measured by elemental analysis by the surface area of the inorganic core calculated from TEM data. (The relevant equation is developed in the ESI) The ligand density is approximately constant among the NPs (1.44 – 1.52 molecules/nm^2), except for the higher value of $MnFe_2O_4$ NPs (1.93 molecules/nm^2). These values

11

are at the low side of the ligand density range (1.2 – 6.6 molecules/nm^2) for long-chain ligands, calculated from the data collected in Ref..[52]
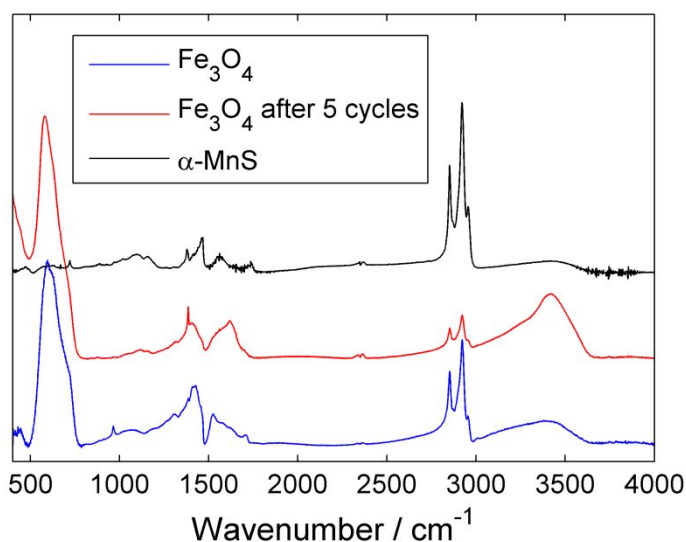

Figure 3. Selected FT-IR spectra of NP catalysts. Blue: fresh Fe_3O_4 NP catalyst. Red: Fe_3O_4 NP catalyst after 5 runs of the **1c** + **2** cycloaddition. Black: α-MnS catalyst.

Table 2. Ligand density of the metal oxide and sulfide nanoparticles.

NP	Surface ligand	C (w/w %)	H (w/w %)	Ligand density (molecules/nm^2)
Fe_3O_4	Oleic acid	3.75	0.59	1.44
$CoFe_2O_4$	Oleic acid	10.77	9.48	1.52
$MnFe_2O_4$	Oleic acid	14.41	13.28	1.93
MnO	Stearic acid	6.12	6.68	1.45
α-MnS	Stearic acid	1.84	2.03	1.51

3.2 Azide-alkyne cycloadditions

Because of the well-known relevance of the azide-alkyne cycloadditions,[53,54] we decided to investigate the reaction between azides **1** and methyl propiolate **2** or dimethylacetylene dicarboxylate **3** (Figure 4) in the presence of catalytic amounts of the NPs listed in Table 1. The appropriate reaction conditions were established by studying the reaction between the azide **1a** and methyl propiolate **2** in anhydrous toluene (Scheme 1, Table 3), this azide was chosen since further synthetic transformations of cycloaddition products can be envisaged.[55]
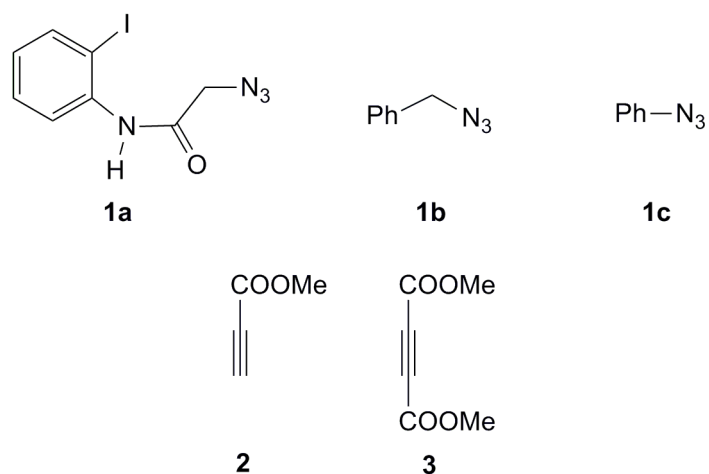
12

Figure 4. Organic reactants for the NP-catalysed azide-alkyne cycloaddition.
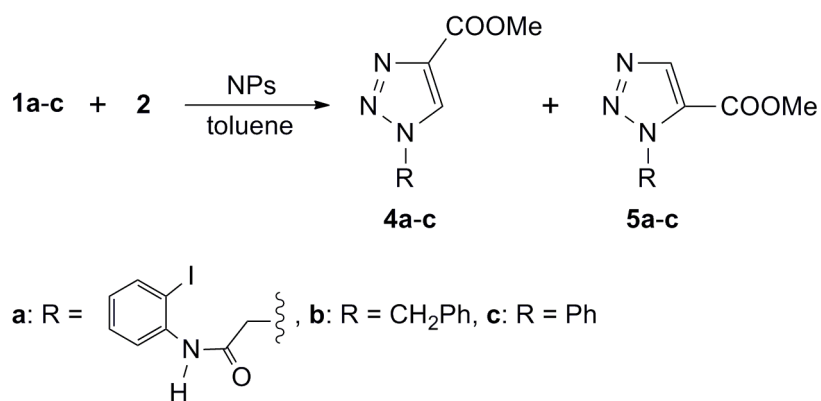
13

Table 3. Cycloaddition between azide **1a** and methyl propiolate **2**.[a]

Entry	NPs	w_{Fe}/w_{1a}[b] (‰)	w_M/w_{1a}[b] (‰)	Time (h)	T (°C)	**4a +5a** (%)	**4a : 5a**
1	—	—	—	240	20	45[c]	51 : 49
2	—	—	—	24	45	57[d]	57 : 43
3	—	—	—	8	95	89	68 : 32
4	Fe_3O_4	21	—	24	20	57[d]	65 : 35[e]
5	Fe_3O_4	21	—	7	45	95	83 : 17[e]
6	Fe_3O_4	21	—	3	75	88	67 : 33[e]
7	Fe_3O_4	21	—	2	95	80	68 : 32[e]
8	$CoFe_2O_4$	10	3.7 (Co)	8	45	93	75 : 25[e]
9	$MnFe_2O_4$	6.4	2.2 (Mn)	6	45	88	71 : 29[e]
10	MnO	—	3.6 (Mn)	7	45	66	65 : 35[e]
11	MnO	—	3.6 (Mn)	40	45	83	65 : 35[e]
12	α-MnS	—	3.1 (Mn)	8	45	62	70 : 30[e]
13	α-MnS	—	3.1 (Mn)	40	45	78	69 : 31[e]

[a]In the presence of iron(III) oleate or bulk Fe_2O_3: (**4a** + **5a**) < 10%, **4a** : **5a** undetermined.
[b]Weight ratio. [c]Unreacted **1a**, 55%. [d]Unreacted **1a**, 40%. [e]As determined by ^{1}H NMR analysis.

As can be seen from Table 3, the "metal free" reaction required long reaction times and yielded poor reactant conversion at room temperature (entry 1). By limiting the reaction time to 24 h at 45°C, the conversion of the reactants was also low (entry 2). At higher temperature (entry 3) the reaction proceeded smoothly as expected for a typical thermal cycloaddition. Similar cycloadditions display similarly high yield when carried out in water.[56] Both reactant conversion and reaction times were satisfactory in the presence of Fe_3O_4 NPs at 45°C (entry 5), while at room temperature some amount of unreacted **1a** was recovered (entry 4). At higher temperatures, good results were obtained (entries 6 and 7) although in these cases any catalytic activity of the Fe_3O_4 NPs can be hardly revealed. Not unexpectedly, the heterogeneous reaction mixture in the presence of bulk Fe_2O_3 did not produce appreciable results. On the other hand, a homogeneous solution of iron(III) oleate were also ineffective, probably due to the crowded, hexacoordinated nature of the iron atom in this complex. In the presence of cobalt and manganese ferrite NPs (entries 8 and 9) at 45 °C, results similar to that observed with Fe_3O_4 NPs were achieved. As far as manganese oxide and sulfide nanoparticles are concerned (entries 10 - 13), their ability to act as catalysts was poorer in comparison to the ferrite NPs. The ligand density is low enough to allow the reactants and products to diffuse to and from the metal oxide surface resulting in a generally good catalytic activity. The better performance of ferrite NPs, in particular Fe_3O_4, must be ascribed to the nature of the surface catalytic in view of the similar ligand density among the NPs. In all cases listed in Table 3 the observed

14

regioselectivity, favouring the 4-cycloadduct in all cases, was higher than of the uncatalysed reaction although the results are not impressive since the regioselectivity is partial and not much different from that of the uncatalysed reaction (*vide infra*).

A related methodology has been published,[57] in which naked maghemite (γ-Fe_2O_3) NPs supported on hydroxyapatite were shown to catalyse the reaction of an organic halide with an alkyne in the presence of NaN_3 in water at 100 °C. This methodology is different from our one as to the nature of the NPs (naked, supported vs. coated, colloidal), the different reactants and solvent, and the reaction temperature. Furthermore, we extended the scope of the reaction and compared the activity of four different oxides and a sulfide.

In order to further investigate the behaviour of the metal oxide and sulfide NPs listed in Table 1, we considered the cycloaddition between benzylazide **1b**, phenylazide **1c** and methyl propiolate **2** (Scheme 1, Table 4). While the reaction times were dependent upon the azide, the reactant conversion was satisfactory for all the NPs. Again, the best conversion and regioselectivity were achieved in the presence of the Fe_3O_4 NPs.

Because of the close similarity of the ^{1}H-NMR spectra of the isomeric cycloadducts **4** and **5**, the independent synthesis of the 4-substituted 1,2,3-triazoles **4** were performed in the presence of copper (I) oxide in toluene (see Experimental Section).

Table 4. Cycloaddition between azides **1b,c** and methyl propiolate **2**.

Entry	NPs	R^1	$w_{Fe}/w_{1b,c}$ (‰)	$w_M/w_{1b,c}$ (‰)	Time (h)	T (°C)	4+5 (%)	4:5
1	—	CH_2Ph	—	—	22	75	85	73 : 27
2	Fe_3O_4	CH_2Ph	48	—	24	45	96	82 : 18[a]
3	$CoFe_2O_4$	CH_2Ph	23	8.5 (Co)	24	45	90	76 : 24[a]
4	$MnFe_2O_4$	CH_2Ph	15	5.1 (Mn)	20	45	88	78 : 22[a]
5	MnO	CH_2Ph	—	8.2 (Mn)	21	45	80	81 : 19[a]
6	α-MnS	CH_2Ph	—	7.1 (Mn)	22	45	84	78 : 22[a]
7	—	Ph	—	—	20	90	99	75 : 25
8	Fe_3O_4	Ph	54	—	8	45	99	82 : 18[a]
9	$CoFe_2O_4$	Ph	26	9.6 (Co)	8	45	95	82 : 18[a]
10	$MnFe_2O_4$	Ph	16	5.5 (Mn)	8	45	95	78 : 22[a]
11	MnO	Ph	—	9.1 (Mn)	8	45	92	74 : 26[a]
12	α-MnS	Ph	—	7.9 (Mn)	8	45	95	77 : 23[a]

[a]As determined by ^{1}H NMR analysis.

15

By submitting azide **1a** to the reaction with dimethylacetylenedicarboxylate **3** (DMAD), the cycloadduct **6** was obtained quantitatively in the presence of both Fe_3O_4 and $MnFe_2O_4$ at 20 °C (Scheme 2, Table 5). The uncatalysed cycloaddition also occurred in the same conditions requiring longer reaction times. Notwithstanding it is known that Huisgen cycloadditions usually occur at high temperature,[58] this latter result should be related to the high dipolarophilic aptitude of DMAD. The obtainment of the 1,2,3-triazole **6** represents a dissimilarity with respect to Sharpless' "click" azide-alkyne cycloaddition since it is well-known that it does not occur onto 1,2-disubstituted acetylenes. However, a few examples of Cu(I) complexes have been shown to catalyse the cycloaddition to internal alkynes.[59]
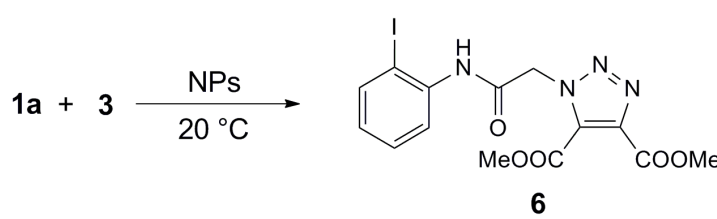
Scheme 2. 1,2,3-Triazole **6** obtained from the cycloaddition between azide **1a** and DMAD **3** in the presence of NPS (see also Table 5)

Table 5. Cycloaddition between azide **1a** and DMAD **3**.

Entry	NPs	w_{Fe}/w_{1a} (‰)	w_{Mn}/w_{1a} (‰)	Time (h)	T (°C)	6 (%)
1	—	—	—	96	20	72
2	Fe_3O_4	5	—	22	20	99
3	$MnFe_2O_4$	6	2	20	20	91
4	—	—	—	4	95	95
5	Fe_3O_4	5	—	1	95	99

The recycling of the NPs was studied for the cycloaddition of **1c** to **2** catalysed by Fe_3O_4 NPs. We performed two series of experiments. The first one follows a conventional protocol: the NPs were magnetically recovered, washed, and immediately dispersed in fresh solvent. In the second series, the magnetically recovered NPs were washed, dried, and weighted before dispersion in fresh solvent in order to measure the loss of NPs due to manipulation. Figure 5 shows the cycloaddition yield for 5 cycles. The isolation yield, as measured in the conventional recycling experiments, decreases with recycling and falls below 50% of the initial value at the fifth cycle.

From the second series of experiments, we learned that the NP mass decreases after each cycle due to manipulation (see ESI, Figure S3). However, it was not possible to envisage the presence of iron in the mother solution *i.e.* in the cycloadducts mixtures. It is likely that the tiny amount of Fe_3O_4 NPs (5.5 mg_{Fe} per cycle on average, compared to ~750 mg of cycloadducts) was lost by washing of the mother solution with water followed by crystallisation of the crude triazoles. When the isolation yield is scaled by the remaining amount of NPs, it remains constant for four cycles and falls to 80% of the initial value at the fifth cycle. The recycling ability of these NPs is not striking but one should recall that they are cheap and do not present serious waste management problems being composed of biocompatible iron oxide and fatty acids so extended recycling is not as important as for precious or toxic catalysts.
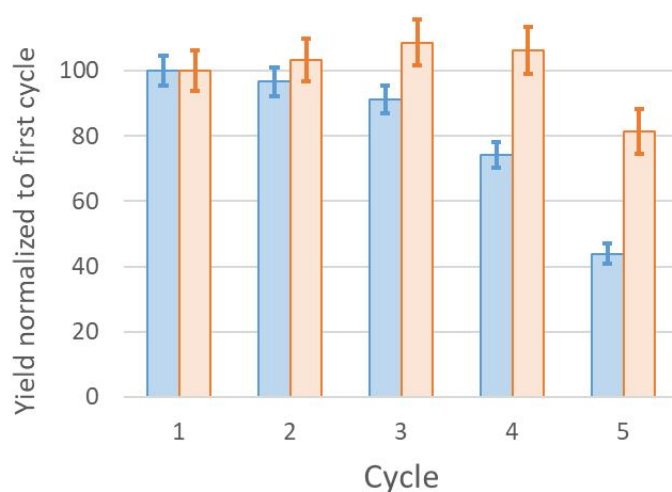
Figure 5. Catalyst recycling for the **1c** + **2** cycloaddition catalysed by Fe_3O_4 NPs. Blue: isolation yield. Orange: isolation yield scaled to the NP loss. All yields are normalized to the value at cycle 1. Error bars represent 2 standard deviations.

To better understand the fate of the catalytic NPs, we analysed Fe_3O_4 NPs after the fifth conventional run by TEM and FT-IR. The FT-IR spectra of fresh and used catalyst are similar (Figure 3), showing that NPs maintain the oleic acid coating. Note that no peaks attributable to **1c** or **2** can be seen. The iron oxide NP core maintained the magnetite structure after the five cycloaddition runs as shown by the ED patterns in Figure 2. TEM images show that the NPs formed large agglomerates with size > 100 nm, in which the Fe_3O_4/oleic acid NPs maintain their individuality (Figure 1). The size of the NPs in unaffected by the use as a catalyst. Thus, in addition to NP loss by manipulation, another cause of decreased activity of the NPs is the agglomeration of the otherwise unchanged NPs that slows down the diffusion of reactants and products to and from the NP surface and lowers the number of catalytic sites available for reaction. These

17

results suggest that the recycling ability of the NPs could be increased by (i) improving the magnetic separation by optimized magnetic field gradients and (ii) sonicating the dispersed NPs

The comparison of the present results with those previously obtained through an uncatalysed cycloaddition must be limited to the reaction between phenylazide **1c** and methyl propiolate **2**. In fact, cycloadducts **4a** and **5a** are novel products, while the 1,2,3-triazoles **4b** and **5b** arising from the reaction of benzylazide **1b** and methyl propiolate **2** were obtained as unique regioisomers in the presence of copper(I) [60] or Cp*RuCl(PPh$_3$)$_2$ [61] catalysts, respectively. As described by Huisgen,[62] phenylazide **1c** reacted with methyl propiolate **2** in the absence of solvent for 12 days at r.t. plus 34 h at 60 °C yielding a mixture of 1-phenyl-4-methoxycarbonyl-1,2,3-triazole **4c** and 5-methoxycarbonyl isomer **5c** in 88 : 12 ratio (83 % combined yield). In a previous report,[63] we investigated the reactive behaviour of phenylazides and methyl propiolate in boiling tetrachloromethane. After 36 h, the **1c**+**2** cycloaddition gave **4c** : **5c** = 75 : 25 (> 96% overall yield). Comparison of these results with Table 4 shows that NP catalysis provides better yield and similar regioselectivity in a much shorter time and at lower temperature. Furthermore, the use of a copper(I) nanocatalyst was able to furnish selectively both the 4-methoxycarbonyl-1,2,3-triazoles **4b**[60] and **4c**.[20] In both cases, yields > 90% were achieved in a few hours at RT.

Compared to the above mentioned Huisgen-type cycloadditions,[58,62] our present results show that the catalytic effect of the studied NPs is such to increase the reaction rate without significantly enhancing the regioselectivity in favour of the 4-substituted triazoles **4**. This behaviour may be ascribed to the reversible formation of a labile azide-NP intermediate that reacts with the alkyne faster than the free azide. The intermediate arises from the interaction between the azide moiety and the uncoordinated metal ion at the NP surface, as shown in Scheme 3. This hypothesis is based on the following considerations. First, we have shown that the catalytic effect is due to the NP surface, most probably to under-coordinated metal ions, since both bulk iron oxide and iron(III) oleate and do not increase the cycloaddition rate. The lack of azide degradation, the absence of by-products, and the occurrence of the cycloaddition to a 1,2-disubstitued acetylene are consistent with the formation of an azide-NP intermediate. It seems likely that organic azides ligate to surface iron ions since both complexes of Fe(III) with the N$_3^-$ anion [64] and transition metal complexes with aromatic azide ligands [65] are known, despite that Fe(III) complexes with organic azide ligands have not been reported (at the best of our knowledge). Ligation of the alkyne ester to surface iron ions is unlikely as Fe(III) complexes with alkynes or esters seem to be of very minor importance.

However, further investigations would be desirable to unravel the details of the mechanistic features concerned to the catalytic activity of the mentioned nanoparticles. In order to get further support to the

18

proposed mechanism of the NP-catalysed azide-alkyne cycloaddition, we carried out DFT calculations that are reported in the next subsection.
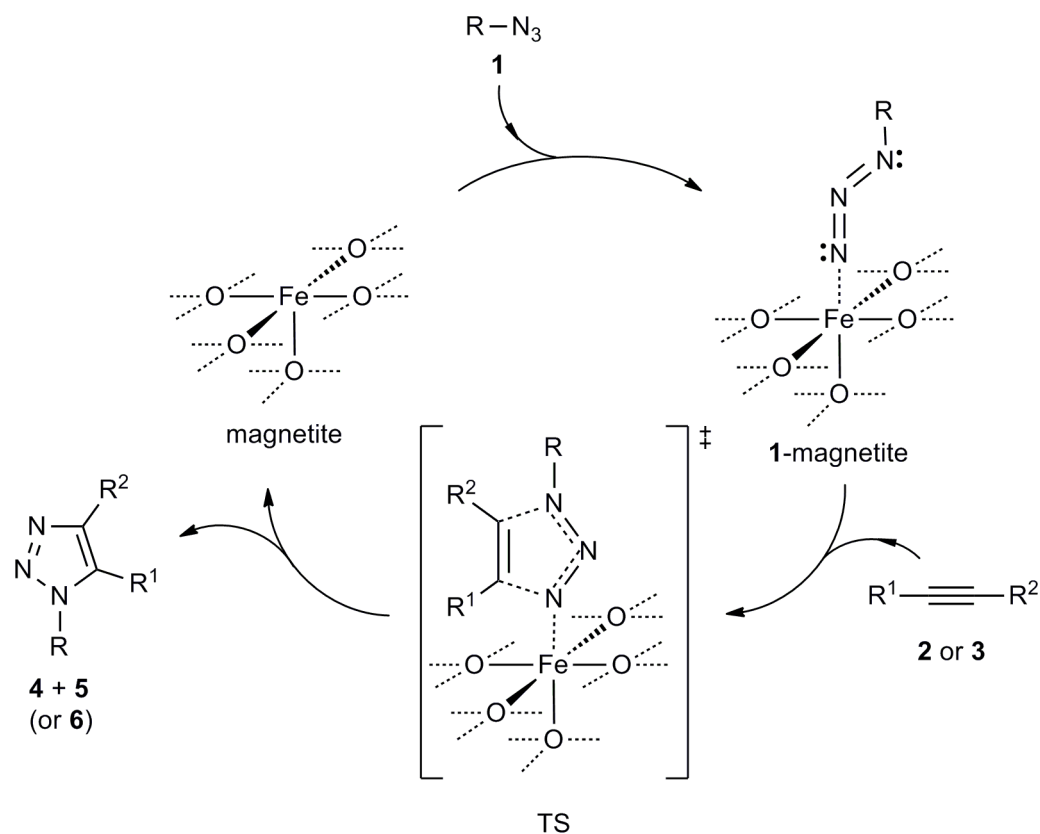
Scheme 3. Proposed catalytic cycle for the NP-catalysed cycloaddition between azide **1** and alkyne **2** in the presence of magnetite NPs. The key step is the adsorption of the azide onto an under-coordinated Fe site at the NP surface. For the sake of clarity, we pictured a single transition state structure but it is understood that both regioisomeric transition states occur. A similar cycle is thought to be effective for mixed ferrites, MnO, and MnS.

3.3 Computational results

DFT calculations were carried out to assess the plausibility of our working hypothesis that the increased reaction rate is related to the adsorption of the azide on the NP surface *via* the interaction between the azido group and under-coordinated surface metal ions. Theoretical computations focused on the cycloaddition of phenylazide **1c** to methyl propiolate **2** catalysed by iron oxide NPs. The problem was attacked in two ways. First, we employed a periodic model where **1c** is ligated to an under-coordinated iron(III) ion at the (100) surface of a magnetite (Fe_3O_4) slab. Periodic calculations with full geometric relaxation provides a description of the electronic structure of the **1c**-magnetite system allowing us to discuss the NP catalytic effect using a frontier molecular orbital (FMO) approach. Since periodic

19

calculations do not allow one to locate transition states (TSs), we secondly used simple molecular models (neutral $Fe(OH)_3$ [40] or $Fe_2(OH)_4$ fragments ligated to **1c**) to calculate the regioisomeric TSs of the **1c** + **2** reaction.
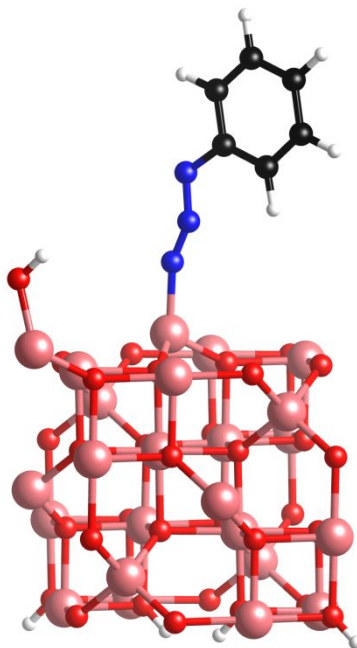

Figure 6. Minimum-energy structure of the **1c**-magnetite adsorption complex. Colour code is as follows. White: hydrogen; black: carbon; blue: nitrogen; red: oxygen; pink: iron.

Figure 6 shows the unit cell of the magnetite (100) surface adopted in the periodic computations and the **1c** azide molecule adsorbed in its minimum energy conformation. We are confident that the results discussed below do not significantly depend on the surface orientation.

According to the FMO approach, reactivity is enhanced when the energy gap between the highest occupied (HOMO) and the lowest unoccupied molecular orbital (LUMO) of the reactants decreases. In molecular systems, the available electronic states correspond to a set of discrete orbital energies. In periodic systems, available electronic states can be found in extended energy intervals (bands) and are collectively pictured by a continuous curve representing the density of available states (DOS). The larger the DOS in a given energy range, the larger the number of states accessible to electrons. We note here that, since magnetite is a magnetic material with a different number of spin-up and spin-down electrons, *ab initio* computations provide two distinct sets of electronic states and hence two different DOS, one for each spin component. To get clear evidence of the energy range where the orbitals of a given atom group contribute significantly to global electronic states, we projected the DOS of **1c**-magnetite onto the orbitals of azide nitrogens, phenyl carbons and the iron atom interacting with **1c**. The analysis conducted below

20

safely assumes that the reaction between **1c**-magnetite and **2** involves electronic states with significant orbital contribution coming from the -N$_3$ (**1c**) and the –C≡C– (**2**) moieties.

The DOS of **1c** adsorbed onto the (100) ferrite surface is shown in Figure 7 along with the orbital energies of the isolated **2** and **1c** molecules, while relevant HOMO – LUMO gaps have been collected in Table 6. For the isolated molecules, we have highlighted the MOs with a large contribution from the reactive moieties –N$_3$ (blue, **1c**) and –C≡C– (black, **2**). For the **1c**-magnetite system, the contributions to the DOS from azide nitrogens (blue), phenyl carbons (grey) and the iron atom interacting with **1c** (red) show where the electronic states relevant to the reaction are located. Pictures of relevant electronic states of **2**, **1c**, and **1c**-magnetite can be found in the ESI (Figure S4).

Table 6. Computed HOMO-LUMO energy gaps (eV) for selected systems.

System	spin component	ΔE [HOMO(**1c**) – LUMO(**2**)]	ΔE [HOMO(**2**) – LUMO(**1c**)]
1c + **2** (gas phase)	both	3.2	4.7
1c-magnetite + **2**	down (minority)	3.3	3.4
1c-magnetite + **2**	up (majority)	2.5	3.5

As can be seen in Table 6, the HOMO-LUMO gaps between **1c** and **2** are 3.2 and 4.7 eV, indicating HOMO-dipole control. Adsorption of **1c** onto the magnetite surface produces marked effects on its electronic structure, which affect the HOMO-LUMO gaps (Figure 7). The overlap of azide and iron peaks in the DOS shows that the molecular states of **1c** hybridize with states located on the magnetite iron atoms (see the states pictured in Figure S5 in the ESI).
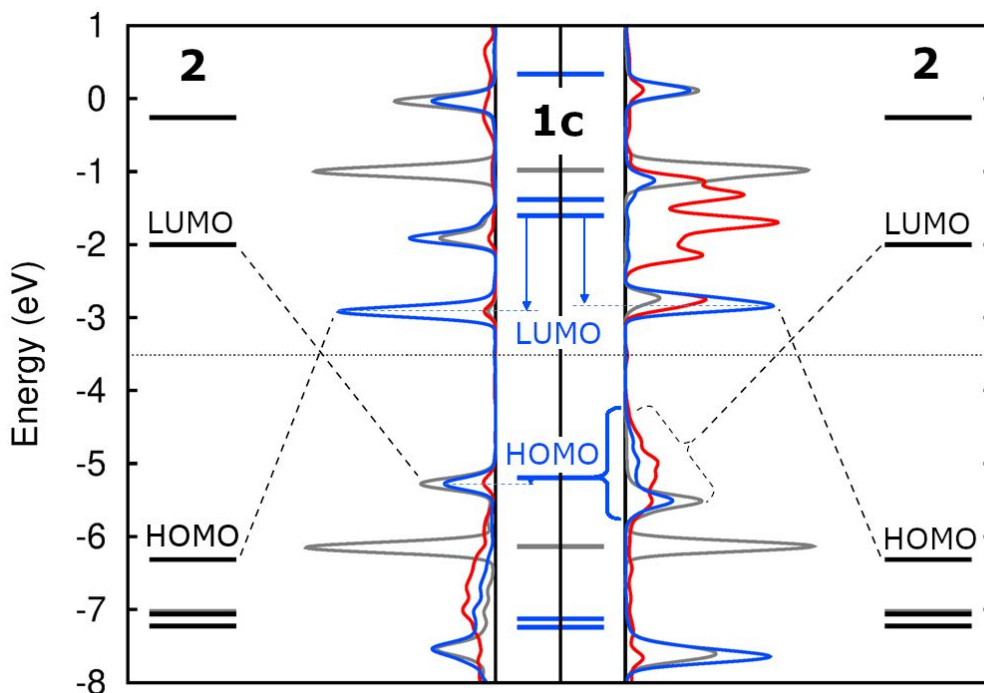
21

Figure 7. Electronic states of isolated **1c** and the **1c**-magnetite complex compared with the states of **2**. The states of isolated **1c** (middle) and **2** (left and right ends) are represented as thick lines. The states of isolated **1c** having large contribution from the $-N_3$ moiety are blue and the states of having large contribution from the $-C \equiv C-$ moiety are black. The density of states (DOS) of spin down (left panel) and spin up (right panel) electrons of the magnetite-**1c** complex are portrayed as continuous curves. Contributions from different moieties are color coded as follows. Blue: azide nitrogens, grey: phenyl carbons, red: iron atom interacting with **1c**. The Fermi level is displayed as a dotted horizontal line (electronic states below the Fermi level are occupied, states above it are empty). The energy shift of the **1c** HOMO and LUMO upon adsorption are indicated by blue arrows. Relevant HOMO-LUMO interactions are highlighted with dashed lines.

As concerns the spin-down electronic states (left panel), we note that the peak corresponding to the HOMO(**1c**) state slightly mixes with Fe orbitals, and its energy slightly lowers with respect to the gas-phase (−0.1 eV). A little hybridization among Fe and N states occurs also for the LUMO(**1c**) peak, leading to a much larger energy shift of about −1.3 eV. Consistently, upon adsorption of **1c** onto magnetite, the HOMO(**1c**) – LUMO(**2**) gap changes slightly with respect to the isolated molecules (see Table 6), while the HOMO(**2**) – LUMO(**1c**) drops from 4.7 to 3.4 eV.

The hybridization of **1c** frontier orbitals with spin-up magnetite states is stronger and more intriguing. The LUMO(**1c**) orbital hybridizes with states at the surface of magnetite, giving rise to a peak at about −

22

2.8 eV. The HOMO(**1c**) strongly mixes with magnetite states giving rise to a broad band of HOMO-like azide-iron states ranging from –5.5 eV to about –4.5 eV. The spin-up HOMO-LUMO energy gaps between **1c**-magnetite and **2** drop to 2.5 [HOMO(**1c**) – LUMO(**2**)] and 3.5 eV [HOMO(**2**) – LUMO(**1c**)], values much smaller than those of the **1c** + **2** reaction. These spin-up **1c**-magnetite hybrid electronic states, which contain large contributions from the -N_3 moiety, provide a faster HOMO-dipole controlled reactivity channel.

The computational results on the periodic model thus suggest that the adsorption of azide **1c** on the magnetite surface is likely to increase the cycloaddition rate because of lower energy gaps for both spin-down (azide-like orbitals) and spin-up (hybrid orbitals) electrons. It is less clear what effect adsorption might have on the regioselectivity since HOMO-dipole control is weaker for magnetite-adsorbed **1c** ($\delta\Delta E$ = 1.1 and 1.0 eV) than for isolated **1c** ($\delta\Delta E$ = 1.5 eV).

To gain more insight, we then turned to the investigation of the relevant TSs in the above delineated simple molecular model. The geometry of the regioisomeric TSs of **1c**-Fe(OH)$_3$ + **2** and **1c**-Fe$_2$(OH)$_4$ + **2** optimized at the OPBE/LANL2/LANL2DZ level are shown in Figure 8. (The **1c** + **2** TSs and the **1c**-Fe(OH)$_3$ and **1c**-Fe$_2$(OH)$_4$ adducts can be found in the ESI, Figure S6).
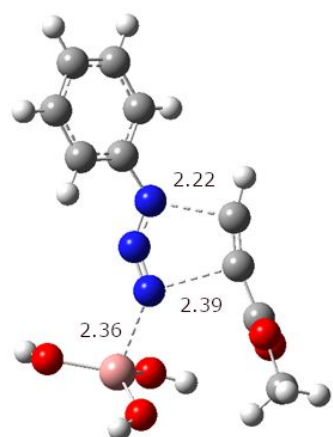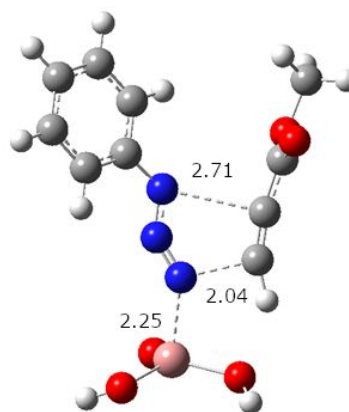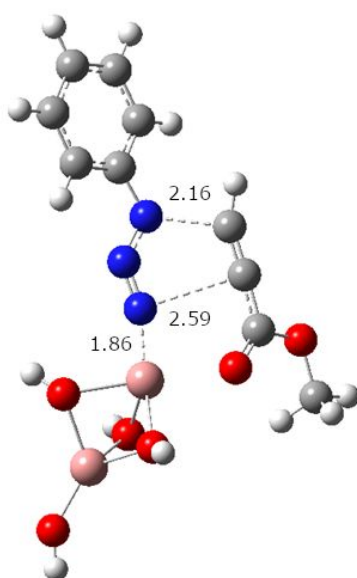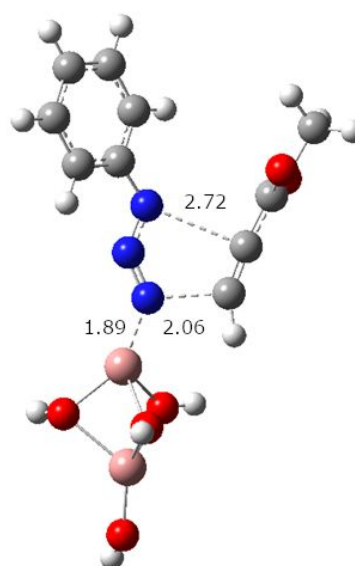
Figure 8. Structure of the regioisomeric transition states of the **1c**-Fe(OH)$_3$ + **2** and **1c**-Fe$_2$(OH)$_4$ + **2** reactions. Relevant distances are given in angstrom. Colour code is as follows. White: hydrogen; grey: carbon; blue: nitrogen; red: oxygen; pink: iron.

The presence of the Fe-O clusters does not affect much the TS structures. With respect to the **1c** + **2** case, the TS leading to **4** is more symmetrical than that leading to **5** and the length of the forming bonds changes by less than 0.1 Å, except for one case. The activation energy $E^{\ddagger} = E(\text{TS}) - E(\textbf{1c}) - E(\textbf{2})$ for the cycloadditions between **2** and both ligated and non-ligated **1c** leading to the **4** and **5** cycloadduct are collected in Table 7. The ligation of **1c** to Fe-O clusters decreases the TS energy of both regioisomeric pathways leading to a significant increase of the reaction rate, in agreement with experiments. However,

24

the data are inconsistent with respect to regioselectivity. One model favours the **4** cycloadduct whereas the other one favours the **5** cycloadduct. This is not unexpected due to (i) the simplistic models employed and (ii) the high accuracy (< 1 kcal/mol) needed to predict the regioselectivity. The computational results based on the molecular model systems support the FMO analysis of the periodic model calculations. We can thus conclude that DFT calculations support the hypothesis that the observed catalytic effect is due to the coordination of **1c** to an under-coordinated iron ion at the NP surface.

Table 7. DFT (OPBE/LANL2/LANL2DZ) activation energy $E^{\ddagger}$ (kcal/mol) for the 4- and 5-regioisomers of the cycloaddition between **2** and both ligated and unligated **1c**.

	4	5
1c	17.2	17.1
1c-Fe(OH)$_3$	15.0	13.1
1c-Fe$_2$(OH)$_4$	10.1	16.1

4. Conclusions

A novel protocol for the catalysed azide-alkyne cycloaddition has been developed, which involves upon Earth-abundant, first-row transition metal oxides and sulfide nanocatalysts. These solvent-dispersible, inexpensive magnetic nanoparticles allowed milder reaction conditions and better product yields compared to the corresponding examples of the classic Huisgen reaction. The regioselectivity of the catalysed cycloaddition towards the 4-cycloadduct was to some extent improved with respect to the thermal process, and the reaction to 1,2-disubstituted acetylenes was proved to be feasible. Experimental and computational results support the hypothesis that the reaction rate increase is due to enhanced reactivity of the adduct between the azide and an under-coordinated iron ion at the surface of the NPs with respect to the free azide.

Conflicts of interest

There are no conflicts of interest to declare.

5. References

1. D. Wang, D. Astruc, *Chem. Soc. Rev.,* 2017, **46**, 816-854.

2. S. Shylesh, V. Schünemann, W. R. Thiel, *Angew. Chem. Int. Ed.*, 2010, **49**, 3428-3459.

3. A. Padwa, in *Comprehensive Organic Synthesis*, *Vol. 4*, (Ed. B. M. Trost, I. Fleming and M. F. Semmelhack), Pergamon Press, Oxford, 1991, pp. 1069-1109.

4. A. Michael, *J. Prakt. Chem*., 1893, **48**, 94-95.

5. R. Huisgen, *Proc. Chem. Soc*., 1961, 357-396.

6. R. Huisgen, *Angew. Chem. Int. Ed. Engl*., 1963, **2**, 565-598.

7. R. Huisgen, *Angew. Chem., Int. Ed. Engl*., 1963, **2**, 633-696.

8. C. W. Tornøe, C. Christensen, M. Meldal, *J. Org. Chem*., 2002, **67**, 3057-3064.

9. V. V. Rostovtsev, L. G. Green, V. V. Fokin, K. B. Sharpless, *Angew. Chem., Int. Ed*., 2002, **41**, 2596-2599.

10. B. C. Boren, S. Narayan, L. K. Rasmussen, L. Zhang, H. Zhao, Z. Lin, G. Jia, V. V. Fokin, *J. Am. Chem. Soc*., 2008, **130**, 8923-8930.

11. L. K. Rasmussen, B. C. Boren, V. V. Fokin, *Org. Lett*., 2007, **9**, 5337-5339.

12. J. R. Johansson, T. Beke-Somfai, A. Said Stålsmeden, N. Kann, *Chem. Rev*., 2016, **116**, 14726-14768.

13. W. Song, N. Zheng, *Org. Lett*., 2017, **19**, 6200-6203

14. W. G. Kim, M. E. Kang, J. B. Lee, M. H. Jeon, S. Lee, J. Lee, B. Choi, P. M. S. D. Cal, S. Kang, J.-M. Kee, G. J. L. Bernardes, J.-U. Rohde, W. Choe, S. Y. Hong, *J. Am. Chem. Soc*., 2017, **139**, 12121-12124.

15. S. Bräse, C. Gil, K. Knepper, V. Zimmermann, *Angew. Chem. Int. Ed*., 2005, **44**, 5188-5240.

16. *Organic Azides: Syntheses and Applications*, (Ed. S. Bräse, K. Banert), John Wiley & Sons, Ltd., Chichester, 2010, pp. 389-490.

17. S. Pålhagen, R. Canger, O. Henriksen, J. A. van Parys, M.-E. Rivière, M. A. Karolchyk, *Epilepsy Res*., 2001, **43**, 115-124.

18. J. Diot, M. I. García-Moreno, S. G. Gouin, C. Ortiz Mellet, K. Haupt, J. Kovensky, *Org. Biomol. Chem.*, 2009, **7**, 357-363.

19. J. M. Aizpurua, R. M. Fratila, Z. Monasterio, N. Perez-Esnaola, E. Andreieff, A. Irastorza, M. Sagartzazu-Aizpurua, *New J. Chem.*, 2014, **38**, 474- 480.

20. G. Molteni, C. L. Bianchi, G. Marinoni, N. Santo, A. Ponti, *New J. Chem.*, 2006, **30**, 1137-1139.

21. T. Jin, M. Yan, Y. Yamamoto, *ChemCatChem.*, 2012, **4**, 1217-1229.

22. F. Alonso, Y. Moglie, G. Radivoy, *Acc. Chem. Res.*, 2015, **48**, 2516-2528.

23. M. B. Gawande, A. Goswami, F.-X. Felpin, T. Asefa, X. Huang, R. Silva, X. Zou, R. Zboril, R. S. Varma, *Chem. Rev.*, 2016, **116**, 3722−3811.

24. M. Gholinejad, N. Jeddi, *ACS Sustainable Chem. Eng.*, 2014, **2**, 2658-2665.

25. S. Kaur, V. Bhalla, M. Kumar, *Chem. Commun.*, 2015, **51**, 526-529.

26. R. Hudson, C.-J. Li, A. Moores, *Green Chem.*, 2012, **14**, 622-624.

27. Z. Zhang, C. Dong, C. Yang, D. Hu, J. Long, L. Wang, H. Li,Y. Chen, D. Kong, *Adv. Synth. Catal.* 2010, **352**, 1600-1604.

28. F. Chahdoura, C. Pradel, M. Gómez, *ChemCatChem*, 2014, **6**, 2929-2936.

29. H. Woo, H. Kang, A. Kim, S. Jang, J. C. Park, J. C.; S. Park, B.-S. Kim, H. Song, K. H. Park, *Molecules*, 2012, **17**, 13235-13252.

30. S. Ishikawa, R. Hudson, A. Moores, C.-J. Li, *Heterocycles*, 2012, **86**, 1023-1030.

31. B. Kumar, K. H. V. Reddy, B. Madhav, K. Ramesh, Y. V. D. Nageswar, *Tetrahedron Lett.*, 2012, **53**, 4595-4599.

32. M. R. Decan, S. Impellizzeri, M. L. Marin, J. C. Scaiano, *Nat. Commun.*, 2014, **5**, 4612.

33. J. E. Hein, V. V. Fokin, *Chem. Soc. Rev.*, 2010, **39**, 1302-1315.

34. A. M. Ferretti, A. Ponti, G. Molteni, *Tetrahedron Lett.*, 2015, **56**, 5727-5730.

35. R. Hudson, Y. Feng, R. S. Varma, A. Moores, *Green Chem.*, 2014, **16**, 4493-4505.

36. C. Della Pina, M. Rossi, A. M. Ferretti, A. Ponti, M. Lo Faro, E. Falletta, *Synthetic Met.*, 2012, **162**, 2250-2258.

37. A. Gervasini, C. Messi, A. Ponti, S. Cenedese, N. Ravasio, *J. Phys. Chem. C*, 2008, **112**, 4635-4642.

38. A. Gervasini, C. Messi, P. Carniti, A. Ponti, N. Ravasio, F. Zaccheria, *J. Catal.*, 2009, **262**, 224-234.

39. M. Tejeda-Serrano, J. R. Cabrero-Antonino, V. Mainar-Ruiz, M. López-Haro, J. C. Hernández-Garrido, J. J. Calvino, A. Leyva-Pérez, A. Corma, *ACS Catal.*, 2017, **7**, 3721-3729.

40. G. Molteni, A. M. Ferretti, S. Mondini, A. Ponti, *J. Nanopart. Res.*, 2018, **20**, 79.

41. a) L. Menini, M. C. Pereira, L. A. Parreira, J. D. Fabris, E. V. Gusevskaya, *J. Catal.*, 2008, **254**, 355-364; b) B. Sahoo, S. Kumar Sahu, S. Nayak, D. Dharaa, P. Pramanik, *Catal. Sci. Technol.*, 2012, **2**, 1367-1374.

42. M. Kazemi, M. Ghobadi, A. Mirzaie, *Nanotech. Rev.*, 2017, **7**, 43-68.

43. P. Calcagnile, D. Fragouli, I. S. Bayer, G. C. Anyfantis, L. Martiradonna, P. D. Cozzoli, R. Cingolani, A. Athanassiou, *ACS Nano*, 2012, **6**, 5413−5419.

44. H. Zhu, S. Zhang, Y. -X. Huang, L. Wu, S. Sun, *Nano Lett.*, 2013, **13**, 2947-2951.

45. E. Capetti, A. M. Ferretti, V. Dal Santo, A. Ponti, *Beilstein J. Nanotechnol.*, 2015, **6**, 2319-2329.

46. J. M. Soler, E. Artacho, J. D. Gale, A. Garcìa, J. Junquera, P. Ordejòn, D. Sànchez-Portal, *J. Phys. Cond. Matt.*, 2002, **14**, 2745-2779.

47. H. Liu, C. Di Valentin, *J. Phys. Chem. C*, 2017, **121**, 25736-25742.

48. M. Swart, *J. Chem. Theory Comput.* 2008, **4**, 2057-2066.

49. Gaussian 09, revision C.01, M. J. Frisch, G. W. Trucks, H. B. Schlegel, G. E. Scuseria, M. A. Robb, J. R. Cheeseman, G. Scalmani, V. Barone, B. Mennucci, G. A. Petersson, H. Nakatsuji, M. Caricato, X. Li, H. P. Hratchian, A. F. Izmaylov, J. Bloino, G. Zheng, J. L. Sonnenberg, M. Hada, M. Ehara, K. Toyota, R. Fukuda, J. Hasegawa, M. Ishida, T. Nakajima, Y. Honda, O. Kitao, H. Nakai, T. Vreven, J. A. Montgomery, Jr., J. E. Peralta, F. Ogliaro, M. Bearpark, J. J. Heyd, E. Brothers, K. N. Kudin, V. N. Staroverov, R. Kobayashi, J. Normand, K. Raghavachari, A. Rendell, J. C. Burant, S. S. Iyengar, J. Tomasi, M. Cossi, N. Rega, J. M. Millam, M. Klene, J. E. Knox, J. B. Cross, V. Bakken, C. Adamo, J. Jaramillo, R. Gomperts, R. E. Stratmann, O. Yazyev, A. J. Austin, R. Cammi, C. Pomelli, J. W. Ochterski, R. L. Martin, K. Morokuma, V. G. Zakrzewski, G. A. Voth, P. Salvador, J. J. Dannenberg, S. Dapprich, A. D. Daniels, Ö. Farkas, J. B. Foresman, J. V. Ortiz, J. Cioslowski, D. J. Fox, Gaussian, Inc., Wallingford, CT, 2010.

50. S. Mondini, M. Leonzino, C. Drago, A. M. Ferretti, S. Usseglio, D. Maggioni, P. Tornese, B. Chini, A. Ponti, *Langmuir*, 2015, **31**, 7381-7390.

51. S. Mondini, A. M. Ferretti, A. Puglisi, A. Ponti, *Nanoscale*, 2012, **4**, 5356-5372. Pebbles is freely available from the authors, http://pebbles.istm.cnr.it.

52. A. M. Smith, K. A. Johnston, S. E. Crawford, L. E. Marbella, J. E. Millstone, *Analyst*, 2017, **142**, 11-29.

53. W. Lwowski in *1,3-Dipolar Cycloaddition Chemistry*, *Vol. 1*, (Ed. A. Padwa) ,Wiley-Interscience, New York, 1984, pp. 559-652.

54. C.-K. Sha, A. K. Mohanakrishnan in *Synthetic Applications of 1,3-Dipolar Cycloaddition Chemistry Toward Heterocycles and Natural Products*, *Vol. 59* (Eds. A. Padwa, W. H. Pearson) John Wiley & Sons, Inc., New York, 2002, pp. 623-679.

55. G. Molteni, *Heterocycles*, 2013, **87**, 1765-1773.

56. (a) Z. Li, T. S. Seoa, J. Ju, *Tetrahedron Lett*. 2004, **45**, 3143-3146; (b) Z.-X.Wang, H.-L. Qin, *Chem. Commun*. 2003, 2450-2451.

57. S. R. Kale, S. S. Kahandal, M. B. Gawande, R. V. Jayaram, *RSC Adv.*, 2013, **3**, 8184-8192.

58. R. Huisgen, R. Grashey, M. Seifeld, W. Wallbillich, H. Knupfer, R. Schmidt, *Ann. Chem.*, 1962, **653**, 105 - 113.

59. (a) S. Díez-González, A. Correa, L. Cavallo, S. P. Nolan, *Chem. Eur. J.*, 2006, **12**, 7558-7564; (b) N. Candelon, D. Lastécouères, A. K. Diallo, J. Ruiz Aranzaes, D. Astruc, J.-M. Vincent, *Chem. Commun.*, 2008, 741-743; (c) S. C. Sau, S. R. Roy, T. K. Sen, D. Mullangi, S. K. Mandal, *Adv. Synth. Catal.*, 2013, **355**, 2982-2991.

60. H. A. Orgueira, D. Fokas, Y. Isome, P. C.-M. Chan, C. M. Baldino *Tetrahedron Lett.* 2005, **46**, 2911-2914.

61. T. Farooq, L. K. Sydnes, K. W. Tornroos, B. E. Haug *Synth.* 2012, **44**, 2070-2078.

62. R. Huisgen, R. Knorr, L. Moebius, G. Szeimies, G. *Chem. Ber*. 1965, **98**, 4014-4021.

63. G. Molteni, A. Ponti *Chem. Eur. J*. 2003, **9**, 2770-2774.

64. N. Wiberg, E. Wiberg, A. F. Holleman *Anorganische Chemie*, De Gruyter, Berlin, 2016, 103rd ed., Band 2, Teil C, Kapitel XXIX, p. 1953.

65. S. Cenini, E. Gallo, A. Caselli, F. Ragaini, S. Fantauzzi, C. Piangiolino, *Coord. Chem. Rev.*, 2006, **250**, 1234-1253.